

To the Graduate Council:

I am submitting herewith a thesis written by Jason Bane entitled “The EMC Effect in A=3 Nuclei.” I have examined the final paper copy of this thesis for form and content and recommend that it be accepted in partial fulfillment of the requirements for the degree of Doctor of Philosophy, with a major in Nuclear Physics.

Nadia Fomin, Major Professor

We have read this thesis
and recommend its acceptance:

Jamie Coble

Kate Jones

Thomas Papenbrock

Soren Soreson

Accepted for the Council:

Carolyn R. Hodges

Vice Provost and Dean of the Graduate School

To the Graduate Council:

I am submitting herewith a thesis written by Jason Bane entitled “The EMC Effect in A=3 Nuclei.” I have examined the final electronic copy of this thesis for form and content and recommend that it be accepted in partial fulfillment of the requirements for the degree of Doctor of Philosophy, with a major in Nuclear Physics.

Nadia Fomin, Major Professor

We have read this thesis
and recommend its acceptance:

Jamie Coble

Kate Jones

Thomas Papenbrock

Soren Soreson

Accepted for the Council:

Carolyn R. Hodges

Vice Provost and Dean of the Graduate School

(Original signatures are on file with official student records.)

The EMC Effect in $A=3$ Nuclei

A Thesis Presented for
The Doctor of Philosophy
Degree
The University of Tennessee, Knoxville

Jason Bane

May 2018

© by Jason Bane, 2018
All Rights Reserved.

Contents

List of Tables	v
List of Figures	vi
1 Introduction	1
1.1 Electron scattering	2
1.1.1 Deep inelastic scattering	5
1.2 EMC Effect	6
1.3 MARATHON	9
2 Experimental Setup	10
2.1 Thomas Jefferson Lab	10
2.1.1 CEBAF	10
2.1.2 Hall A	12
2.2 Target	17
2.3 High Resolution Spectrometers	17
2.3.1 Vertical Drift Chambers	19
2.3.2 Scintillators	20
2.3.3 Cherenkov	20
2.3.4 Shower Calorimeter	20
2.3.5 Pion Rejector	20
2.3.6 FPP Chambers	20

2.4	Trigger Setup	20
2.5	DAQ - Data Acquisition System	20
2.6	Kinematic Settings	20
3	Calibration	21
3.1	Beam Line	21
4	Data Analysis	24
5	Results	25
6	Simulation	26
6.1	Investigation	26
6.2	Transformation	27
6.3	Results	29
7	Conclusion	32
	Bibliography	33

List of Tables

List of Figures

1.1	Simple Feynman diagram of an electron scattering from a proton [7].	3
1.2	Graph of the ratio of A/D structure functions vs x for Carbon [10].	7
1.3	EMC effect from EMC, SLAC, and BCDMS [15]	8
1.4	Graph of the ratio of A/D structure functions vs x for Carbon [10].	9
2.1	Schematic Layout of CEBAF.	11
2.2	A 3D drawing of Hall A.	12
2.3	A schematic layout of the beam line in Hall. [1]	13
2.4	BPM design diagram, from JLab instrumentation group. Beam direction is from left to right [21].	14
2.5	BPM design diagram, looking down the beam line[21].	14
2.6	Hall A Current Monitor components [4].	16
2.7	A view of both the left(top) and right(bottom) detector stacks inside the left and right HRS [1].	18
2.8	A sketch of the two VDC planes in the HRSs with a particle traveling through the detector at 45° . [6].	19
3.1	A schematic layout of a harp fork [21]	22
3.2	The X and Y position for a Bulls eye scan for BPM calibration.	23
6.1	Example of the electron beam(red) with a energy of 2.5 GeV and the proton(blue) with angle of 45° in respect to the electron and with a momentum of 0.5 GeV/c.	27

6.2	Vector representations of the momentum for the incoming electron(red) and target proton(blue) with units of GeV for each phase of their transformations before scattering.	28
6.3	Vector representations of the momentum for the incoming electron(red) and target proton(blue) with units of GeV for each phase of their transformations after scattering).	30
6.4	Simulation results for fixed momentum protons. Three runs with unique proton momentum.	31

Chapter 1

Introduction

Understanding the world around us is the goal of every scientist, from the chemist that experiments with the formation of atoms to the geologist exploring the process of rock formations. Nuclear physicists focus on studying the fundamental constituents of matter, the building blocks of nature. Physicists use scattering experiments at accelerator facilities, like CERN in Switzerland, DESY in Germany, BATES in Massachusetts, JLAB in Virginia, and many others, to study the protons and neutrons and their constituents that make up a nucleus. These experiments allow physicists to observe the internal structure of the nucleus and to investigate the interactions between the quarks and gluons. Many of the experiments are designed to confirm existing results while also expanding on unique ideas.

In the last century, there have been numerous breakthroughs in the fields of nuclear and particle physics. Rutherford discovered the proton by bombarding light nuclei with alpha particles to produce



This reaction allowed Rutherford to conclude that the Hydrogen nucleus was a constituent of an atomic nucleus [16]. In the late 1950s, experimental results published

by W. McAllister and R. Hofstadter exposed some of the internal structure of the proton [7, 14]. The European Muon Collaboration(EMC) produced results in the early 1980s showing a differences between the internal structure of the deuterium nucleus and Iron [18, 10]. The data received from scattering experiments using alpha particles contain information about the target, the beam, and the interaction between the two. Deciphering and analyzing this data can be convoluted because the cross-section contains information about the internal structure of the target and the beam along with the interaction and forces between the two [16].

1.1 Electron scattering

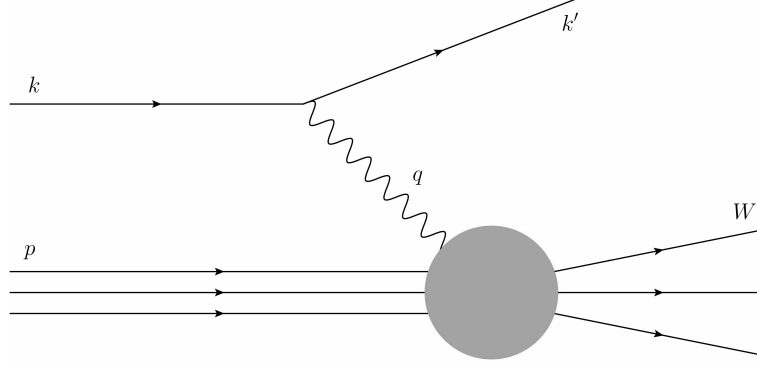
In order to remove some of the complexity in scattering experiments, one may employ highly relativistic electrons. Electrons being point-like particles without any internal structure allow the elimination of some of the analysis difficulties with using alpha particles in scattering experiments due to their complex internal structure. Electrons and the target nucleus, nucleon, or quarks interact via the exchange of a virtual photon. Using quantum electrodynamics (QED), these interactions can accurately be described by the well known electromagnetic interaction. Higher order terms of this process contribute very little due to the coupling constant $\alpha \approx 1/137$, being much smaller than one.

Figure 1.1 represents an electron scattering from a proton. The incoming or incident electron's four-momentum is described as $k = (E, \vec{k})$ and the scattering electron's four-momentum is represented by $k' = (E', \vec{k}')$. The exchange of the virtual photon in this electromagnetic interaction is defined by the four-momentum transfer q :

$$Q^2 \equiv -q^2 = 4EE' \sin^2(\theta/2). \quad (1.2)$$

In equation 1.2, E and E' are the electron energy before and after the scattering interaction. θ is the angle that describes the deflection of E' from the electron's original path.

Figure 1.1: Simple Feynman diagram of an electron scattering from a proton [7].



Along with Q^2 , the variables ν , W , and x_B are used to narrate the evolution of the electron scattering process. ν , defined as $p \cdot q/M$. In the rest frame of the target, ν can be described by:

$$\nu = E - E'. \quad (1.3)$$

Simply, ν is the magnitude of energy loss by the electron during the scattering interaction. The invariant mass of the system, W , defines the hadronic state produced by the scattering event.

$$W^2 \equiv (q + p)^2 = M^2 + 2M\nu - Q^2. \quad (1.4)$$

A scattering event with the invariant mass equal to the square of the mass of the nucleon, (M^2), falls in the regime of elastic scattering. W above M^2 will transform the scattering interaction from an elastic scattering to inelastic scattering due to the excited state of the scattered byproduct. x_B , the Bjorken scaling variable is a dimensionless quantity that measures the inelasticity of a scattering process. x_B is defined as: $x := \frac{Q^2}{2M\nu}$.

The intrinsic likelihood of an event with a certain Q^2 , ν , and W is defined by the scattering cross section. An electron scattering off of a target with a charge of $Z * e$ can be described by the Rutherford cross-section. Povh et. al. details the Rutherford cross section as:

$$\left(\frac{d\sigma}{d\Omega}\right)_{Rutherford} = \frac{(zZe^2)^2}{(4\pi\epsilon_0)^2 * (eE_{kin})^2 \sin^4(\theta/2)}. \quad (1.5)$$

The electron has a charge (ze) and kinetic energy of E_{kin} [16]. However in the early 1920s, German physicists Stern and Gerlach performed an experiment that confirmed the presence of electron angular momentum. Later a discovery of electron spin was made by Uhlenbeck and Goudsmit. The Rutherford cross-section neglects the spin of the electron and the target. The Mott cross-section is the evolved version of the Rutherford cross-section. It has been modified to include the intrinsic spin of the target and electron. The Mott cross-section can be scribed as:

$$\left(\frac{d\sigma}{d\Omega}\right)_{Mott} = \frac{4Z^2\alpha^2(\hbar c)^2 E'^2}{|\mathbf{q}c|^4} \cos^2(\theta/2) [11, 16]. \quad (1.6)$$

When the results from actual scattering experiments of electrons off nuclei or the nucleons located inside, there is an agreement between the measured cross section and the theoretical Mott cross-section when in the limit of $|\mathbf{q}| \rightarrow 0$. As $|\mathbf{q}|$ climbs furtherer from zero, the experimentally measured cross sections systematically decrease [16]. Increasing the $|\mathbf{q}|$ of an interaction reduces the size of the wavelength of the virtual photon that mediates the electromagnetic interaction and increasing the resolution. The wavelength of this virtual photon is inversely proportional to $|\mathbf{q}|$, the amount of momentum transferred in an electron scattering interaction. The relationship between the wavelength and $|\mathbf{q}|$ can be described by the following: $\lambda = \frac{\hbar}{|\mathbf{q}|}$ [16]. Increasing the amount of momentum transfered in an electromagnetic reaction allows one to study deeper into the nucleus.

Studying the internal structure of a nucleus with the electromagnetic interaction requires increasing the momentum transferred. Pushing $|\mathbf{q}|$ to be comparable with the mass of a nucleon adds more complexity to the details of the scattering interaction. At the appropriate levels of $|\mathbf{q}|$ to study the nucleons in the nucleus, the Mott cross-section equation requires modifications to include additional factors that incorporate information about the target. The Rosenbluth formula is based on the Mott cross section and embraces target recoil, magnetic moment, and charge and current distributions. Povh writes the Rosenbluth formula as:

$$\left(\frac{d\sigma}{d\Omega}\right) = \left(\frac{d\sigma}{d\Omega}\right)_{Mott} * \left[\frac{G_E^2(Q^2) + \tau G_M^2(Q^2)}{1 + \tau} + 2\tau G_M^2(Q^2) \tan^2 \frac{\theta}{2} \right]. \quad (1.7)$$

Equation 1.7 contains $G_E^2(Q^2)$ and $G_M^2(Q^2)$, the electric and magnetic form factors. τ is used in the Rosenbluth formalism to account for the magnetic moment of a nucleon and is defined as: $\tau = \frac{Q^2}{4M^2c^2}$ [16]. In the general case of electron scattering off of a free proton or neutron elastically, the scattered energy of the electron will be a function of the incident electron's energy and the scattered angle of the electron, shown in the following equation.

$$E' = \frac{E}{1 + \frac{E}{Mc^2}(1 - \cos\theta)} \quad (1.8)$$

1.1.1 Deep inelastic scattering

The first generation of electron scattering experiments achieving a significantly large $|\mathbf{q}|$ used a linear accelerator with a 25 GeV maximum beam energy, and following generations increased the total interaction energy to substantially higher thresholds. At these high incident beam energies, individual resonances cannot be separated in the invariant mass spectrum above 2.5 GeV. Observations made into this convoluted invariant mass spectrum has shown that many strongly interacting particles are produced, known as hadrons. Scattering interactions that generate these hadrons are title inelastic scattering. Inelastic scattering events contain the possibility of conceiving additional resultants and increase the complexity of the

scattering interaction. Due to the increase in complexity, an additional degree of freedom has to be included into the scattering cross section. This can be done by slightly modifying the Rosenbluth formula to include the inelastic scattering structure functions $W_1(Q^2, \nu)$ and $W_2(Q^2, \nu)$. This modification is shown in equation, [1.9](#).

$$\frac{d^2\sigma}{d\Omega dE'} = \left(\frac{d\sigma}{d\Omega} \right)_{Mott} \left[W_2(Q^2, \nu) + 2W_1(Q^2, \nu) \tan^2 \frac{\theta}{2} \right] \quad (1.9)$$

Inelastic scattering events occur when the wavelength of the virtual photon is comparable to the radius of the struck nucleon or when $Q^2 R^2 \lesssim 1$. When $Q^2 R^2 \gtrsim 1$, the probe may interact with the charge constituents deep within the nucleon. When the scattering happens off fundamental parts of the proton or neutron, the scattering process is titled deep inelastic scattering(DIS).

[\[19\]](#) [\[12\]](#)

1.2 EMC Effect

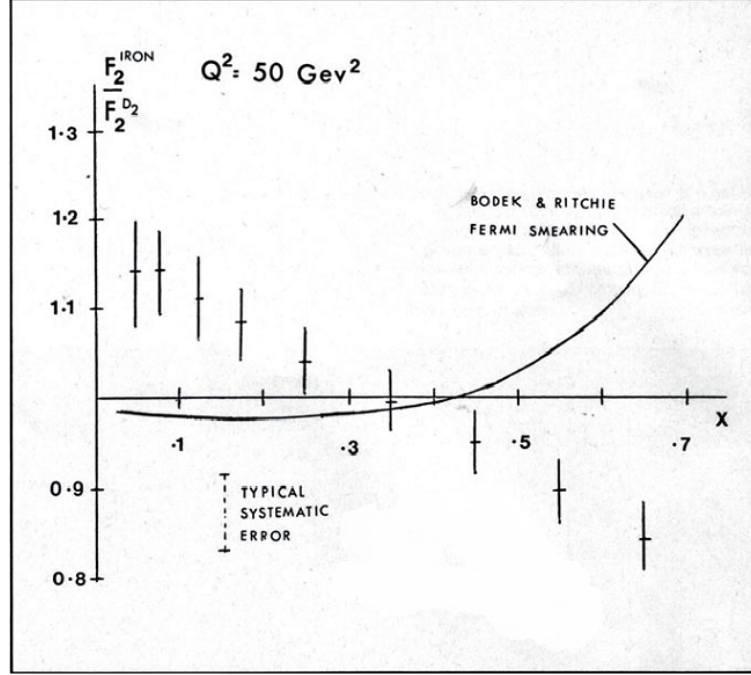
The European Muon Collaboration (EMC) performed a deep inelastic measurement with 120-280 GeV muons on iron and deuteron targets [\[13\]](#). The EMC extracted A/D structure function ratios versus the Bjorken scaling variable, x . The relationship originally expected by the EMC contained the sum of the structure functions of each nucleon in a nucleus. Each nucleus has a certain number of neutrons (N) and a amount of protons (Z). The expected structure function for a nucleus could be written as:

$$F_A = N F_2^N + Z F_2^P. \quad (1.10)$$

The EMC compared the extracted structure functions from iron and deuterium. Their results are shown in [Figure 1.2](#). The $\frac{A}{D}$ structure function ratio showed an unexpected downward slope. This phenomenon was titled the EMC effect. This finding demonstrated to the EMC that their understanding of the nucleus

was incorrect. A nucleon's structure function and thereby, the constituent quark distributions may be altered by the nucleus.

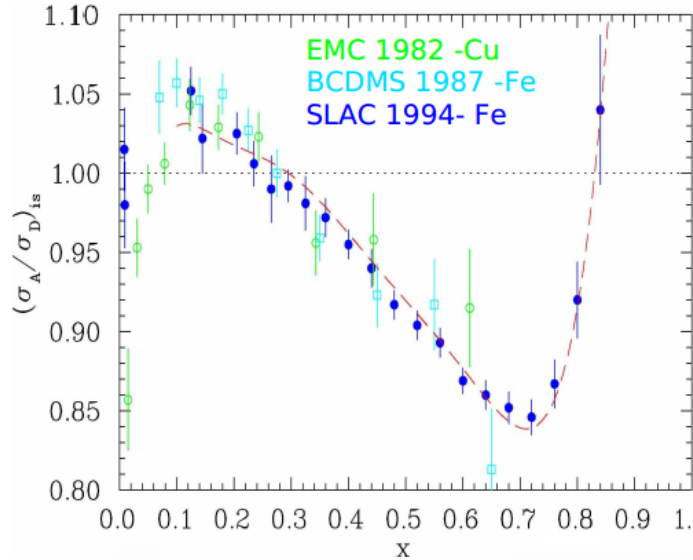
Figure 1.2: Graph of the ratio of A/D structure functions vs x for Carbon [10].



Ever since the European Muon Collaboration discovered the depletion of quarks at high x for $A > 2$ nuclei, physicists have tried to discover its cause. Scientists at SLAC extracted structure function ratios for many nuclei including; ^4He , ^9Be , ^{12}C , ^{27}Al , ^{40}Ca , ^{56}Fe , ^{108}Ag , and ^{197}Au . There were slightly different results for each nucleus. The magnitude of the EMC effect, taken to be the A/D ratio at $x = 0.6$, was found to be different for the various nuclei, and roughly scaled with the size or density of the nuclei. The NMC (New Muon collaboration), another group at CERN, gathered precise data in order to construct the inclusive cross section of deuterium and protons. BCDMS collaboration extracted data for N and Fe structure function ratios. Figure 1.3 shows some of the data from SLAC and BCDMS on the EMC effect for Iron and Cu. Figure 1.4 shows this result from a recent JLab EMC measurement, most precise to date. Many models over the years have been able to reproduce the shape

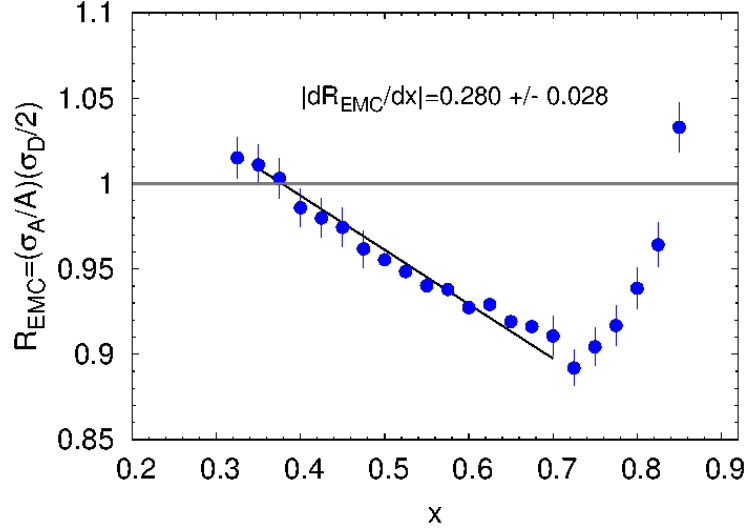
of the A/D ratios. These models can contain traditional nuclear physics effects like momentum distribution or pion-charge contributions. Some models also describe the EMC effect through quark momentum distribution or modification of the internal structure [15, 5, 2, 8, 9]. However, no single model has provided a complete picture of the possible underlying physics. Precise data from Jlab's E03-103 experiment has revitalized this research. This experiment focused on precision measurements in light nuclei and added ^3He as a target nucleus. Instead of taking the A/D ratio at a certain x -value to be the magnitude of the EMC effect, this analysis looked at the slope instead. This eliminated sensitivity to normalization uncertainties.

Figure 1.3: EMC effect from EMC, SLAC, and BCDMS [15]



In Figure , ^9Be was found not to follow the previously observed scaling with nuclear density. This result from Jefferson Lab determined that the previous idea of a dependence on A or nuclear density in the EMC effect to be incorrect [18]. This result spawned a drive to determine another explanation for the EMC effect and understand what clue the ^9Be outlier was providing. The structure of this nucleus is made up of two high-density alpha particles and a single neutron [3]. The regions

Figure 1.4: Graph of the ratio of A/D structure functions vs x for Carbon [10].



of higher density that are contained in a comparatively large volume may be able to explain why ^9Be does not follow the expected trend. This suggests that the EMC effect could be a function of local nuclear density [18].

1.3 MARATHON

Experiment E12-010-102, MARATHON (MeAsurement of the $F_2^n/F_2^p, d/u$ RATios and A=3 EMC Effect in Deep Inelastic Electron Scattering Off the Tritium and Helium MirrOr Nuclei), will use deep inelastic scattering off of the mirror nuclei ^3H and ^3He to measure the EMC effect for both ^3H and ^3He , to determine the ratio of the neutron to proton inelastic structure functions, and to find the ratio of the down to up quark distributions in the nucleon.

Chapter 2

Experimental Setup

2.1 Thomas Jefferson Lab

Thomas Jefferson Lab (Jlab) in Newport News, Virginia hosted the MARATHON experiment in the Fall of 2017 and Spring of 2018. Jlab uses support from the U.S. Department of Energy(DOE) and the state of Virginia to complete the lab's mission of delivering productive research by exploring the atomic nucleus and its fundamental constituents, including precise tests of their interactions. Along with applying an advanced particle accelerator, particle detectors and other technologies to develop new basic research capabilities and to address the challenges of a modern society.

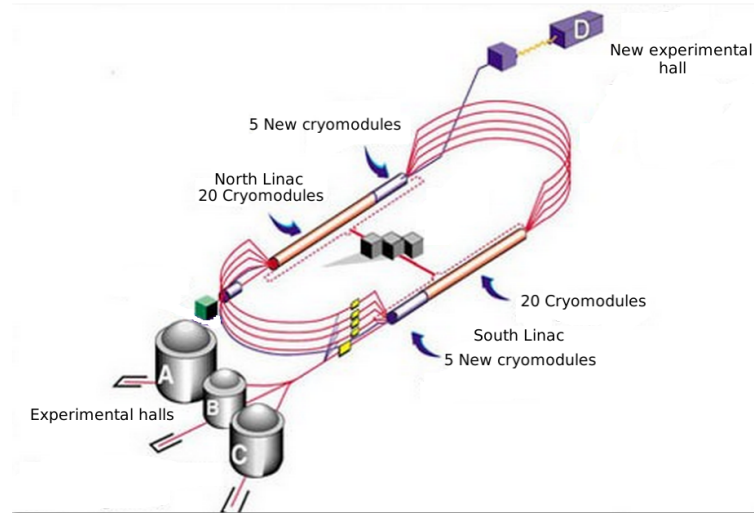
2.1.1 CEBAF

The Continuous Electron Beam Accelerator Facility (CEBAF) was recently upgraded to a 12 GeV accelerator, upgrading it to be able to supply a 11 GeV beam of continuous electrons of up to $200\ \mu\text{A}$ of current to three experimental halls (A,B,C) and 12 GeV to the recently constructed hall D. After being accelerated to 45 MeV by a polarized electron gun or a thermionic injector, the electrons are injected into the North linear accelerator (LINAC), shown in figure [2.1](#). The polarized gun can supply electrons with up to 80% polarization and the polarization direction can be controlled

by a wien filter. To ensure the level of polarization, a 5 MeV Mott polarimeter may be used to measure the level of polarization[1].

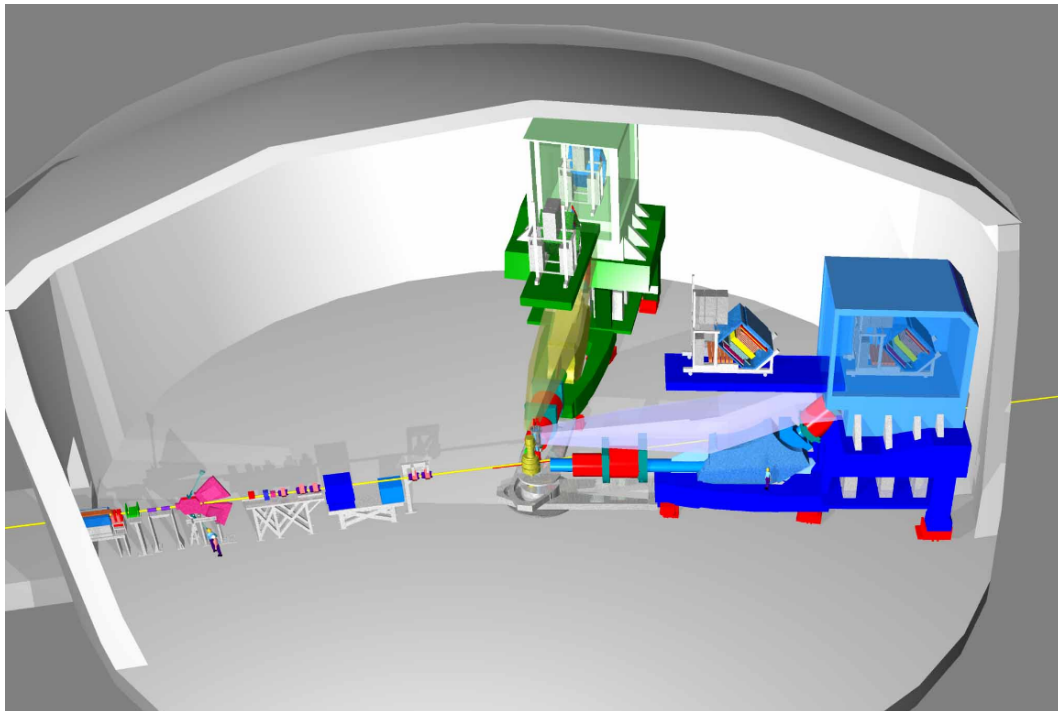
The electrons are conveyed through two LINACs and two bending arcs per complete pass of the accelerator. Electrons traveling to Halls A, B, and C complete a maximum of four and a half revolutions around the accelerator. Electrons going to all D travel through the north LINAC for an extra boost. These particles receive approximately 2.2 GeV in energy for each cycle through the accelerator. The radio frequency (RF) cavities in each LINAC use an oscillating electromagnetic field to supply a force to accelerate the passing electrons. These Niobium RF cavities are cooled to 2 K in order to create conditions that allow the cavities to be superconducting [1].

Figure 2.1: Schematic Layout of CEBAF.



2.1.2 Hall A

Figure 2.2: A 3D drawing of Hall A.

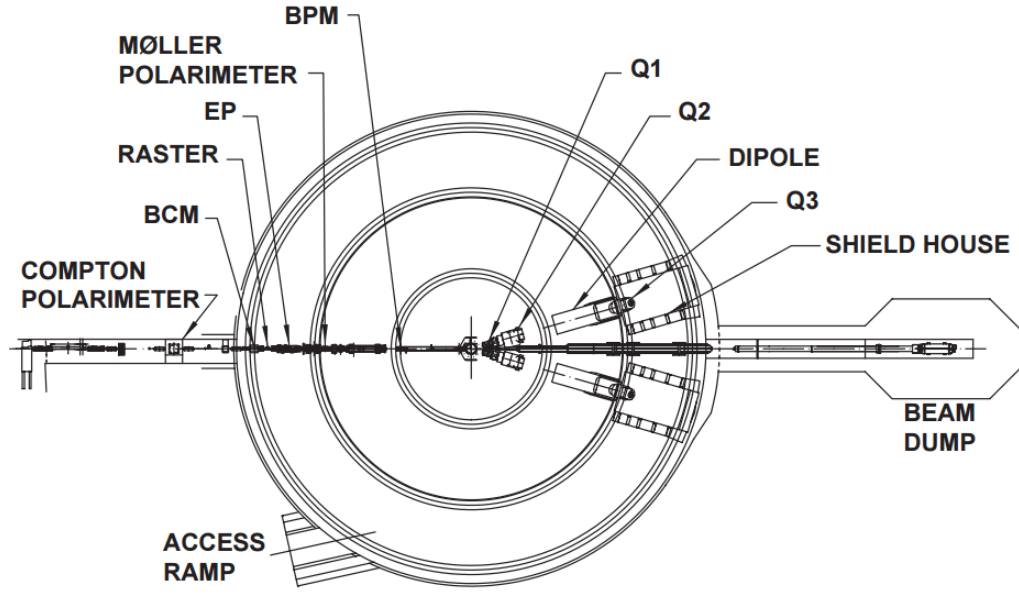


The experimental Hall A and the scientific equipment used were designed for detailed investigations of the internal structure of nuclei. Two high resolution spectrometers in Hall A use the inclusive (e,e') and exclusive $(e,e'p)$ reactions to gain a greater understanding of the structure of the nucleus. Completing detailed studies with high resolution and extreme accuracy requires knowing the beam position, size, energy, current, direction, and polarization when the beam strikes the target. The instrumentation used in the precise measurement of these quantities in Hall A are shown in figure 2.3 [1].

A pair of Beam Position Monitors(BPM)s are used to measure the relative beam position without affecting the beam. The two Hall A BPMs are located at 7.524 m and 1.286 m away from the target. Using the standard difference-over-sum technique, the relative beam position is determined with an accuracy of $100 \mu\text{m}$ with a beam

current of at least $1 \mu\text{A}$ [1]. The BPMs' positional data is recorded in two ways. Every second of beam time, the beam position average over 0.3 seconds is logged into the Experimental Physics and Industrial Control System (EPICS) database. The BPMs also transmit data event-by-event to the CEBAF online Data Acquisition system(CODA).

Figure 2.3: A schematic layout of the beam line in Hall. [1]



The main beam line components of the BPMs consist of four open-ended antennas. Figure 2.4 shows a BPM chamber and figure 2.5 shows the layout of the four antennas as you look down the beam line. In this chamber, the design of three of the four antennas can be seen. The antennas are titled u_+ , u_- and v_+ , v_- . The antennas receive an induced signal as electrons pass to determine the beam position in the u and v directions. The direction of the beam is determined by using the two BPMs in conjunction with timing information provided. The accuracy of the BPMs requires an absolute measurement of the electron beam's position to calibrate the BPMs and a internal input oscillation measurement names twiddle to supply BPM signal coefficients. [17, 21].

Figure 2.4: BPM design diagram, from JLab instrumentation group. Beam direction is from left to right [21].

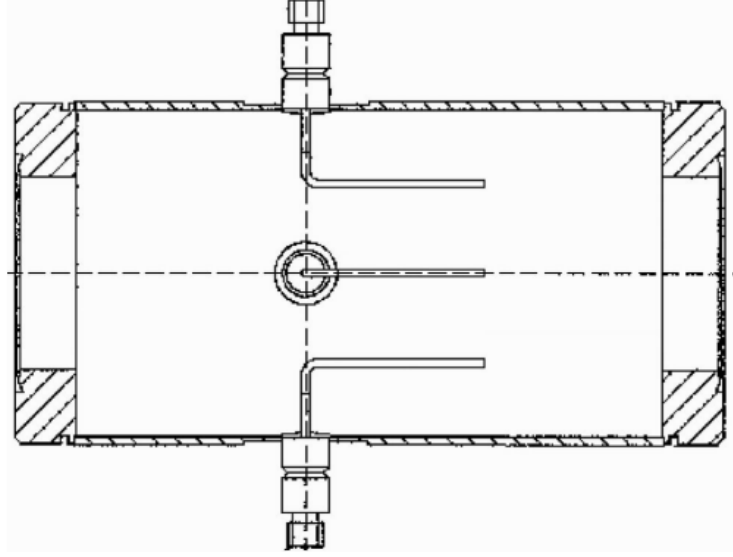
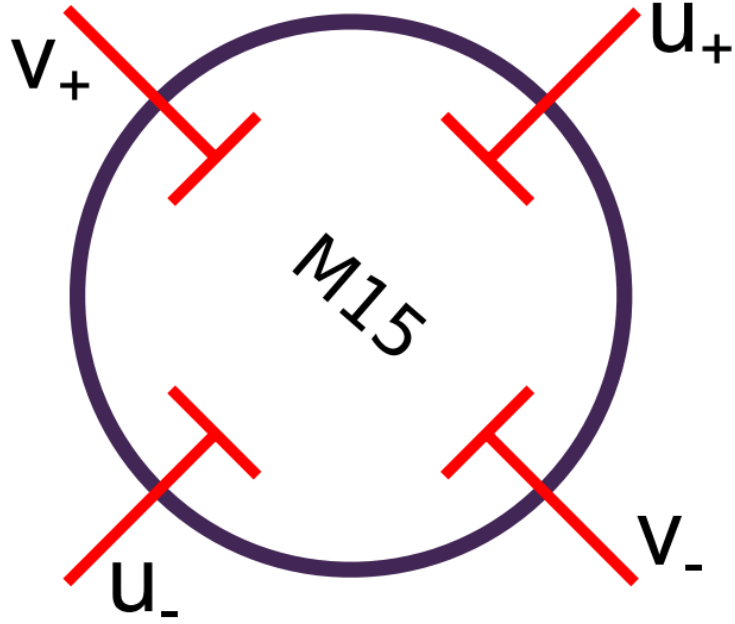


Figure 2.5: BPM design diagram, looking down the beam line[21].



Damage to a target system from intense beam can cause extreme fluctuations in the target's temperature and density. A raster was used to counteract the damage

caused by a focused beam. The raster used two magnetic fields produced by two dipoles to spread the electron beam out. This produces a large rectangle interaction area on the front face of the target container. A triangle wave of 25 kHz was used to control the coils of the dipole magnets. The raster systems are located ≈ 17 meters before the target chamber (upstream of the target[21]). The rasters position can be seen in figure 2.2. Safety constraints administrated by the target group at JLAB limited the minimum size of the raster spot for the MARATHON experiment to two millimeters by two millimeters. This limit was installed has a safety concern for the tritium target.

The Hall A raster system consists of four dipoles. Two dipoles produce magnetic fields in the horizontal direction of the lab frame and two in the vertical. The upstream raster and downstream rasters include one vertical and one horizontal dipole. The relative change in position of the incoming electrons are controlled by the current supplied to the dipoles. In order to obtain the change in beam position due to the rasters, a calibration between the raster current and measured beam position were obtained.

The electron beam energy is located in many of the equations used in an electron scattering experiment. This can cause a noticeable increase in systematic error if the beam energy measurement is not made precisely. At JLAB for the MARATHON experiment, the beam energy was measured in two ways. In Hall A, the beam energy was measured by using the (e,e'p) method. On the beam line, 17 meters upstream from the target an ep scattering chamber is located. The beam was directed into the target containing a rotating 10-30 μm thick tape of CH_2 . The scattering angle of the electron and the recoil angle of the proton are used to determine the beam energy using equation 2.1. Where M_p is the mass of the proton and θ_p, θ_e are the scattered

angle of the proton, electron respectively.

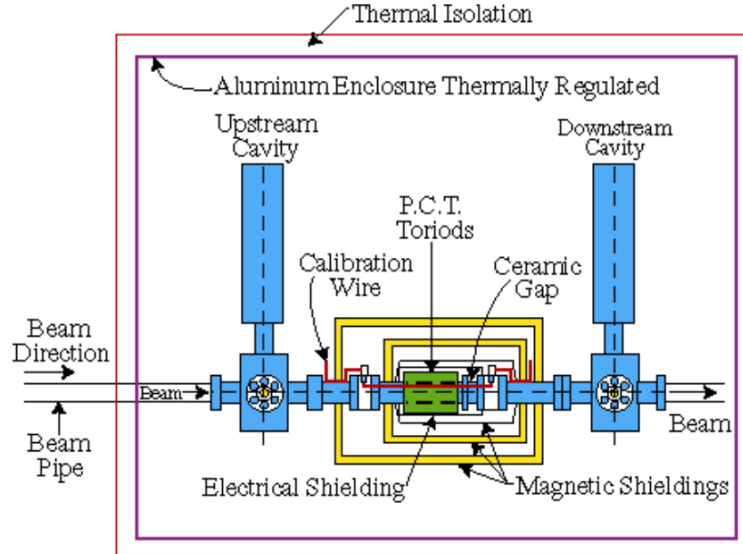
$$E = Mp \frac{\cos\theta_e + \frac{\sin\theta_e}{\tan\theta_p} - 1}{1 - \cos\theta_e} \quad (2.1)$$

The beam energy was also measured using the ark measurement method [7]. This method uses changes in beam position and precise measurements of the magnetic fields around the beam line to determine the energy of the electron beam. The angle at which the electrons are bent through is related to the momentum of the electrons,

$$p = k \frac{\int \vec{B} \cdot d\vec{l}}{\theta}. \quad (2.2)$$

In equation 2.2, p is the momentum of the electrons, θ is the bend angle, and \vec{B} is the magnetic field the electron experiences. Then using the momentum of the electron, the energy of the beam can be extracted. The error on the beam energy measurement is $\delta E/E \approx 2 * 10^{-4}$ [20, 7]. The MARATHON experiment used both methods to accurately determine the electron beam energy.

Figure 2.6: Hall A Current Monitor components [4].



The main process of measuring the scattering yield for a calculation of a cross section looks at finding the ratio of the number of electrons scattered to the number of electrons sent. In order to accurately determine the number of electrons sent to scatter with our target system, Hall A use a highly accurate and non-invasive beam current monitor(BCM). The Hall A BCM has an absolute accuracy of 0.2 percent as long as the current is between 1 and 180 μA . The BCM used in Hall A consists of three main components: a Parametric Current Transformer (PCT) and two pill box cavities. Figure 2.6 shows the components in the Hall A BCM. The BCM produces an RF signal that is proportional to the beam current. An 10 kHz down converter, RMS-to-DC converter, voltage-to-Frequency converter, and a scaler are used to inject the current signal into the Hall A DAQ. A proportionality constants is determine in the calibration process to correctly integrate the charge for a given amount of beam current[4]. After all of the beam passes through these beam line detectors, it will then enter into the target system.

2.2 Target

2.3 High Resolution Spectrometers

Electrons that successfully scatter from the target may end up in the HRS(High Resolution Spectrometers). The HRSs were designed to detect charged particles with a high degree of precision. In order to achieve a high level of resolution in momentum and angle, the HRSs were designed with a magnet configuration of QQD_nQ (Quadrupole, Quadrupole, Dipole, and Quadrupole). The vertical bending dipole provides the field required to transport the scattered particles through the 45° bending angle to the detector hut. The spectrometers were designed to perform various functions which include: triggering the data acquisition system (DAQ) when certain requirements are met, gathering the position and direction of individual particles to reconstruct a track, provide precise timing information, and identify

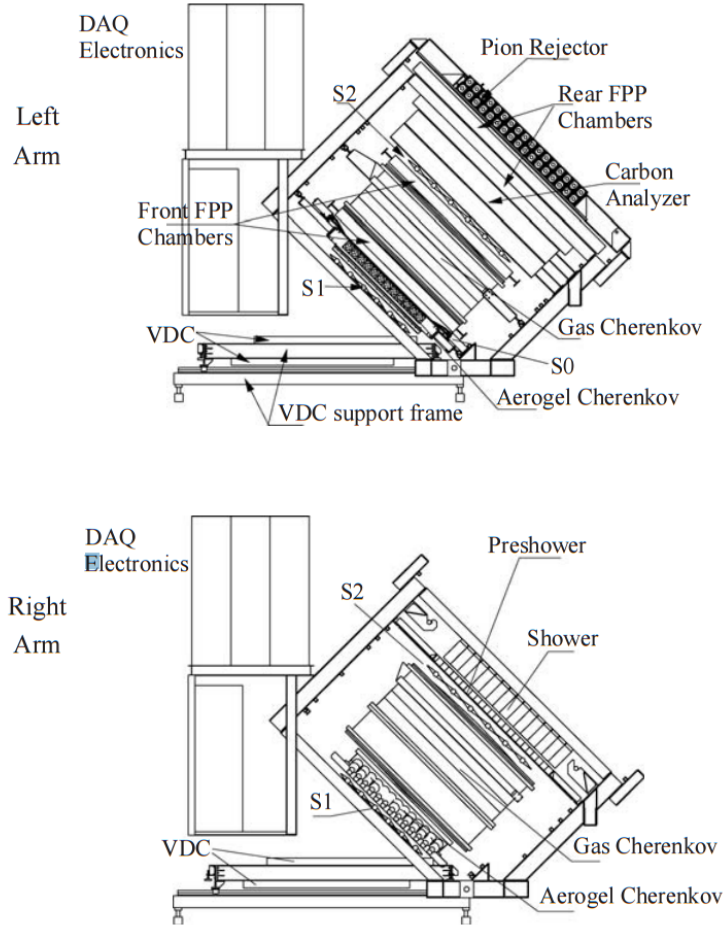


Figure 2.7: A view of both the left(top) and right(bottom) detector stacks inside the left and right HRS [1].

many different particle types that pass through the detector system. Both the Left and Right HRSs contain two planes of Scintillators to function as the main trigger for the detector package. The vertical drift chambers (VDC) that lay at the front of the detector in conjunction with the Shower that lies in the back of the detector provide information for reconstructing the particle tracks and precise timing. Particles are identified by the Cherenkovs, shower calorimeters, and Pion Rejectors that are contained in the left or right HRS. The layout of the individual detectors that make up the left and right detector package are shown in figure 2.7 [1].

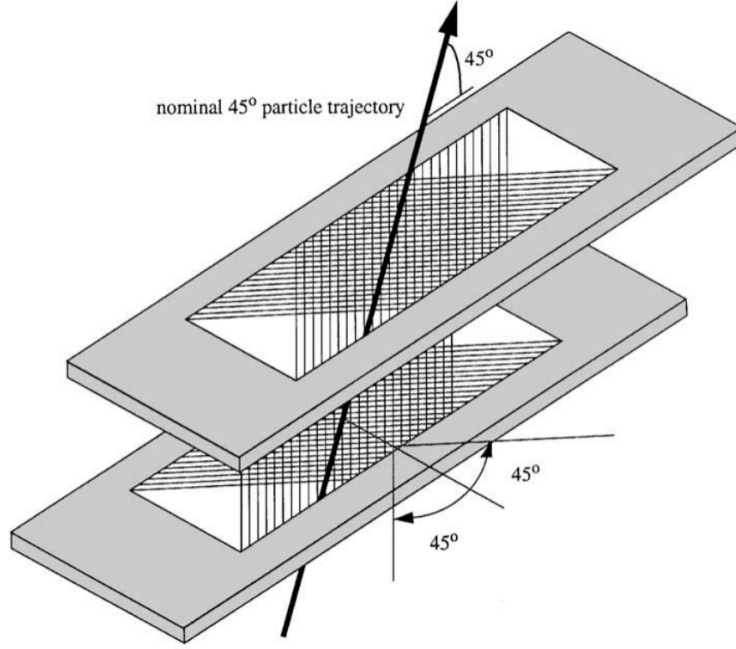


Figure 2.8: A sketch of the two VDC planes in the HRSs with a particle traveling through the detector at 45° . [6].

2.3.1 Vertical Drift Chambers

Each of the spectrometers housed in Hall A contains a vertical drift chamber(VDC). Each VDC contains two planes of crossing sense wires. Shown in figure 2.8, the two planes of the VDC lie a distance of 0.335m apart [6]. The lower plane of the VDC is positioned at the approximate focal plane of the HRS and lies in the horizontal plane of the Hall A coordinate system. The sense wires located in the VDCs cross orthogonally. They are offset by 45° in respect to the dispersive and non-dispersive directions.

[6]

2.3.2 Scintillators

2.3.3 Cherenkov

2.3.4 Shower Calorimeter

2.3.5 Pion Rejector

2.3.6 FPP Chambers

2.4 Trigger Setup

2.5 DAQ - Data Acquisition System

2.6 Kinematic Settings

Chapter 3

Calibration

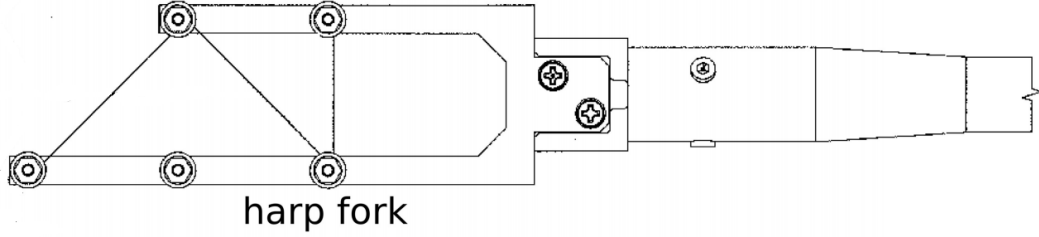
The information provided by the detectors originate through small changes in current and voltage sent through the DAQ electronics. These signals are transformed into useful information through calibration constants. The beam line elements and the individual detector components were calibrate to supply highly precise and accurate data.

3.1 Beam Line

The BPM signal coefficients are determined by a twiddle measurement. An RF module attached to the BPM antennas is used to pass a signal out of each of the antennas, one at a time. This will allow the determination of the conversion factor for the BPM signal to relative beam position. Two harps were used to provide the absolute measurement required for calibrating the BPMs. Figure [3.1](#) contains a drawing of the harps used in Hall A. The harps were moved into the beam line when calibration data is needed, but must be moved out for the production of experimental data because the harp wires are intrusive to the beam operation. The harp forks are aligned perpendicular to the beam line, to allow the harps to be moved in and out of the beam line. Three different wires are used to determine the horizontal and vertical position of the beam. Each wire has one of three orientations: vertical, sloped down

or sloped up. The two sloped wires are angled at 45° relative to the wire frame. As the harp fork is moved into the beam, the wires receive a signal as the beam interacts with the wires. The two sloped wires are used together to determine the vertical position of the beam. The vertical wire is used to determine the horizontal position of the beam [17, 21].

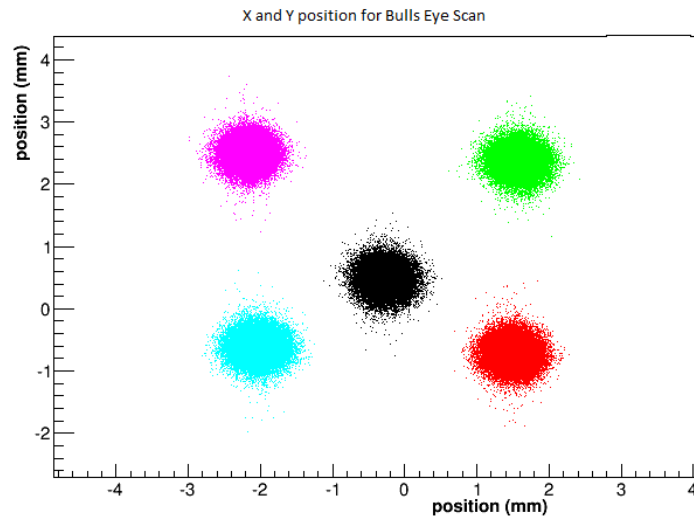
Figure 3.1: A schematic layout of a harp fork [21]



The location of the wires on the harp frame and the position of the harp fork were used to calculate the absolute beam position. The BPM calibration coefficients were determined by using a bulls eye scan, figure 3.2 shows an example of the five positions used to calculate the BPM calibration coefficients. The harp scan results are substituted into equation 3.1 for the X and Y positions. Using all five points and an R^2 regression technique, the coefficients can be determined with great accuracy. These highly accurate BPMs were crucial in reducing systematic error in the final results obtained from this experiment.

$$\begin{pmatrix} X_{position} \\ Y_{position} \end{pmatrix} = \begin{pmatrix} C(0,0) & C(0,1) \\ C(0,0) & C(0,1) \end{pmatrix} * \begin{pmatrix} X_{BPM} \\ Y_{BPM} \end{pmatrix} + \begin{pmatrix} X_{offset} \\ Y_{offset} \end{pmatrix} \quad (3.1)$$

Figure 3.2: The X and Y position for a Bulls eye scan for BPM calibration.



Chapter 4

Data Analysis

Chapter 5

Results

Chapter 6

Simulation

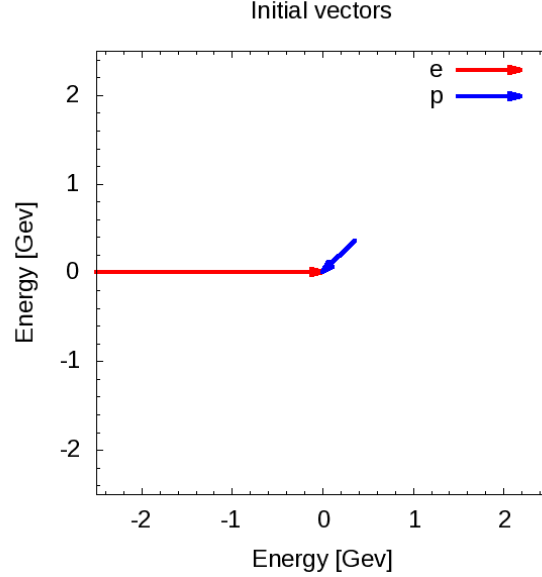
Nuclei are systems of nucleons that interact strongly. The characteristic scale for the nucleons momentum is approximately the Fermi momentum, $k_F \approx 200 - 270 \text{ MeV}/c$ [9]. However because of the strongly repulsive nature of the nucleon-nucleon interaction at short distances prevents two nucleons from laying in close proximity to each other. This strong interaction demands the presence of high-momentum components in the nuclear ground state wave function. A simulation was designed to phenomenologically study the effect of these high-momentum components on the nuclear EMC effect. This program was designed in two phases. The first phase used simple elastic scattering and a single value for the targets momentum to investigate overall effect of different target momentum on the yield in bins of x_B . The second phase of the simulation was created to lay out the effect of using different momentum distributions on the yield for the EMC effect region of x_B , 0.3 to 0.7.

6.1 Investigation

This simulation phenomenologically investigates the effect of a moving target on the EMC effect by scattering a beam of electrons off of a moving proton. The target protons are comprised of a directional vector of 0° to 360° in respect to the incoming electron beam and a momentum between 0 and 1 GeV/c. Figure 6.1 contains a

possible event for the simulation. The electron approaches with 2.5 GeV of energy and collides with a proton moving with a momentum of 0.5 GeV/c with an angle of 45° in respect to the electron trajectory.

Figure 6.1: Example of the electron beam(red) with a energy of 2.5 GeV and the proton(blue) with angle of 45° in respect to the electron and with a momentum of 0.5 GeV/c.



Using conservation of momentum and conservation of energy in elastic collisions, this simulation calculates the final state of the electron and proton after the scattering event by randomly selecting a scattered direction for the electron. The vector representation of the scattered products are shown in figure 6.3a. In order to make these calculations systematic and to study cross sections models the simulation transform each event into the rest frame of the target before scattering.

6.2 Transformation

The Simulation completes a set of Lorentz invariant rotations and boost for each event to transform the lab frame of the electron and proton collision into the rest frame of the proton. First the simulation takes the initial proton and electron vectors

and rotates them to align the proton vector to the horizontal axis, shown in figure 6.2b. This rotation uses the angle between the proton and the electron defined as λ . This allows for a straight forward calculations for the Lorentz factors β and γ and to boost into the rest frame of the target proton, figure 6.2c. Once in the boosted frame, the angle between the electron and the horizontal axis is defined as δ . Right before the simulation starts to calculate the scattered products, it completes one more rotation to align the electron vector with the horizontal axis, figure 6.2d, to make the scattering calculation systematic and unconditional.

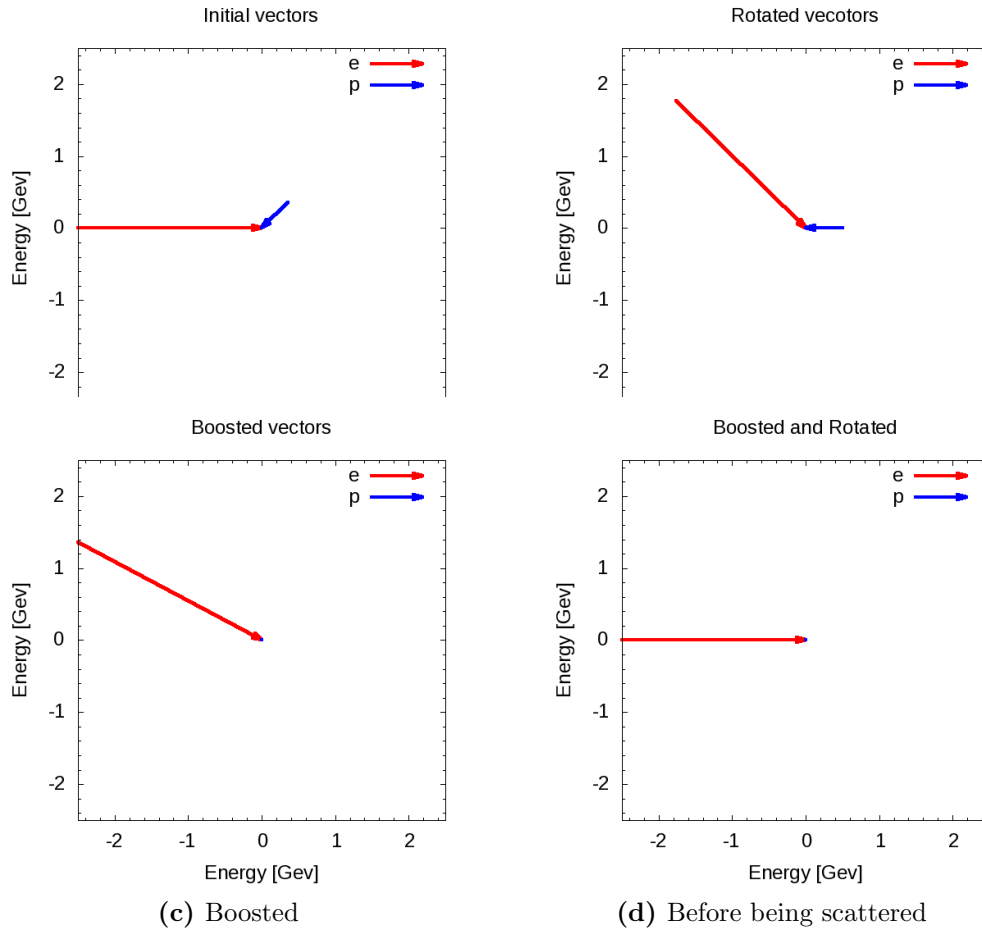


Figure 6.2: Vector representations of the momentum for the incoming electron(red) and target proton(blue) with units of GeV for each phase of their transformations before scattering.

In order to gain a more complete understanding of the scattering products, the program completes a set of transformations to move from the rest frame of the target proton to the beginning lab frame. After the simulation calculates the scattered products it begins to transform back by beginning with a rotation by the angle δ , figure 6.3b. Followed by the inverse of the previously used Lorentz boost. The last transformation, a rotation by λ , transforms the frame back into the lab frame. A proton vector and electron vector in the lab frame are the final products of the simulation. An image of the electron and proton vectors for each transformation can be found in figure 6.3. These vectors allow for calculation of kinematic variables such as Bjorken x and the four-momentum transfer (Q^2). This simulation will complete these steps for many electron and proton combinations.

6.3 Results

This electron scattering simulation produced results for two stages. The first stage used a fixed proton momentum for each run to compare the yield in bins of x_B . Figure 6.4 shows the results for three different runs, each having a unique fixed proton momentum. The red histogram represents a run with a proton momentum of 0 GeV/c. The result is an elastic peak at x_B of one. The blue histogram contains the results having a fixed proton momentum of 0.25 GeV/c. Increasing the initial momentum of the proton spreads the events into two peaks. The scattering interactions that form the peak above 1 x_B are produced by events where the proton's initial directional vector is orientated towards the electron. The events that produce an x_B below 1 have a proton direction pointing away from the electron initially. Doubling the proton's initial momentum from 0.25 GeV to 0.50 GeV causes these peaks to spread out further in x_B .

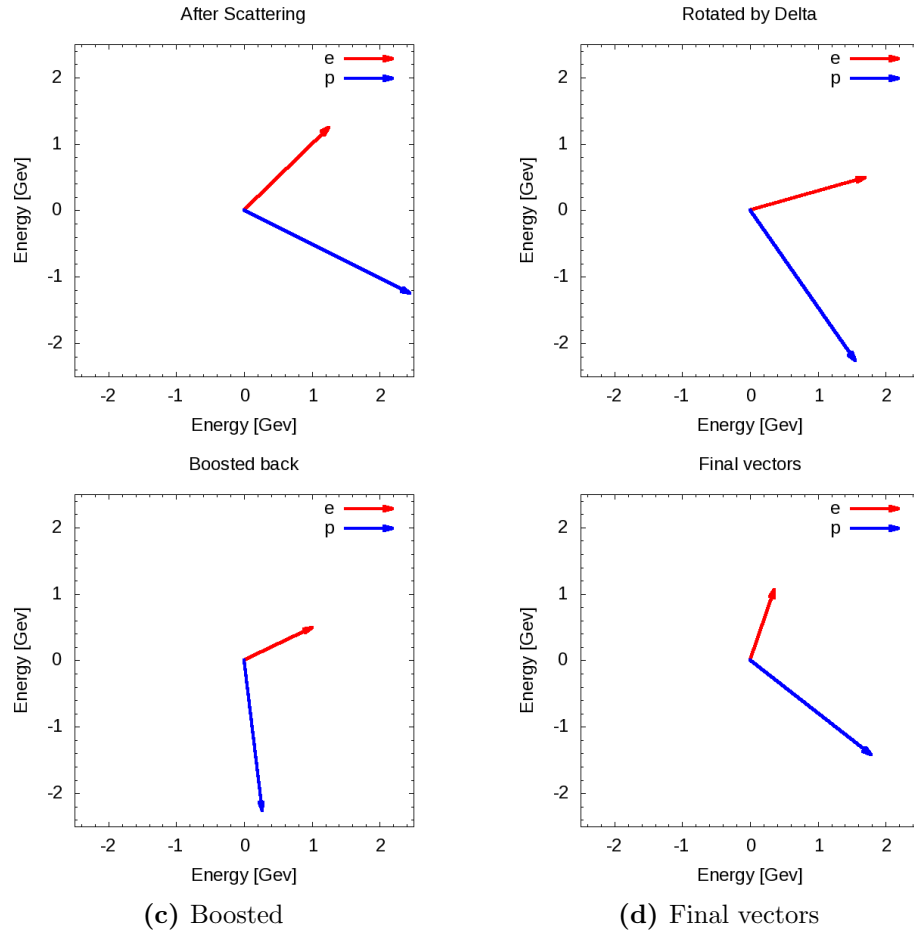
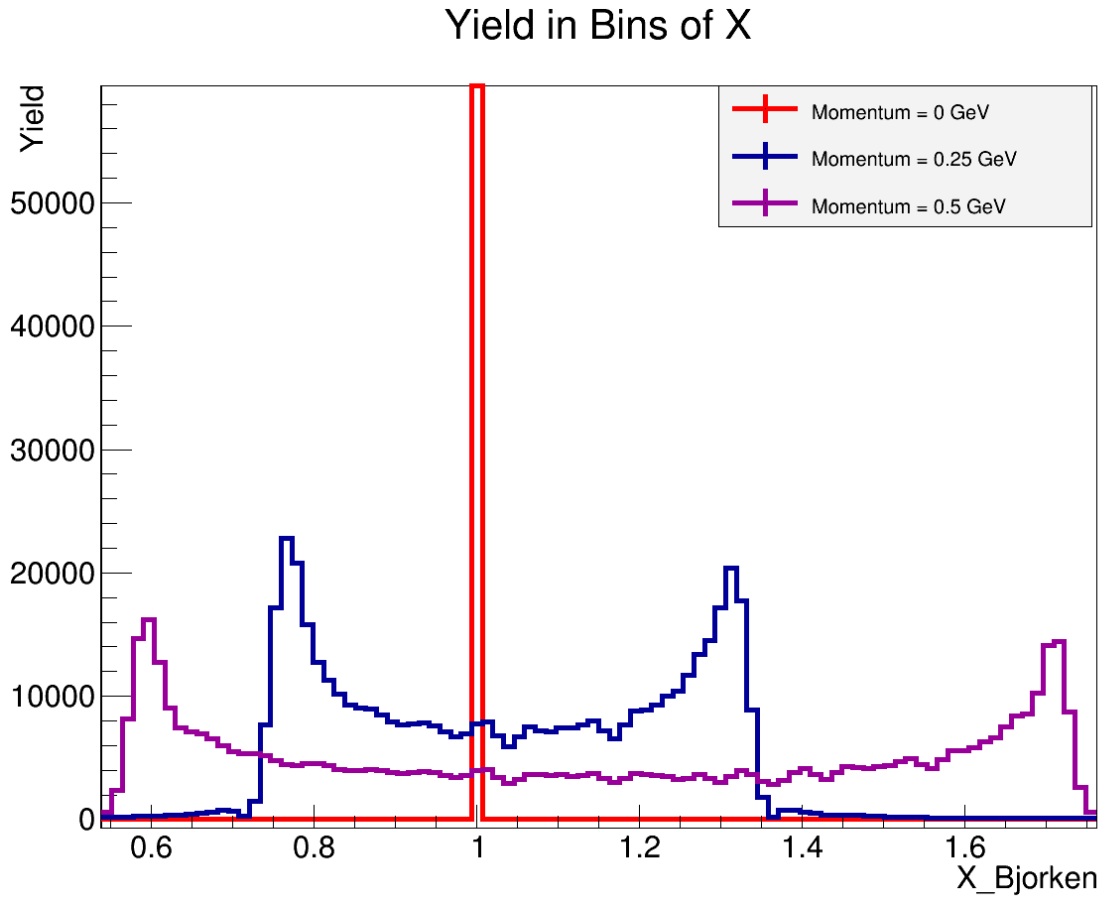


Figure 6.3: Vector representations of the momentum for the incoming electron(red) and target proton(blue) with units of GeV for each phase of their transformations after scattering).

Figure 6.4: Simulation results for fixed momentum protons. Three runs with unique proton momentum.



Chapter 7

Conclusion

Bibliography

Bibliography

- [1] J. Alcorn et al. Basic Instrumentation for Hall A at Jefferson Lab. *Nucl. Instrum. Meth.*, A522:294–346, 2004. [vi](#), [11](#), [12](#), [13](#), [18](#)
- [2] John Arrington, Aji Daniel, Donal Day, Nadia Fomin, Dave Gaskell, and Patricia Solvignon. A detailed study of the nuclear dependence of the EMC effect and short-range correlations. *Phys. Rev.*, C86:065204, 2012. [8](#)
- [3] A. Daniel, J. Arrington, and D. Gaskell. Measurements of the EMC effect in few-body nuclei at large x. *AIP Conf. Proc.*, 1369:98–105, 2011. [8](#)
- [4] J. Denard and J. Sahar. High accuracy beam current monitor system for cebaf’s hall a. Chicago, 2001. Particle Accelerator Conference. [vi](#), [16](#), [17](#)
- [5] J. Edelmann, G. Piller, Norbert Kaiser, and W. Weise. Resonances and higher twist in polarized lepton nucleon scattering. *Nucl. Phys.*, A665:125–136, 2000. [8](#)
- [6] K.G. Fissum et al. Vertical drift chambers for the hall a high-resolution spectrometers at jefferson lab. *Nuclear Instruments and Methods in Physics Research Section A: Accelerators, Spectrometers, Detectors and Associated Equipment*, 474(2):108 – 131, 2001. [vi](#), [19](#)
- [7] David J. Flay. *Measurements of the Neutron Longitudinal Spin Asymmetry A_{1n} and Flavor Decomposition in the Valence Quark Region*. PhD thesis, Temple University, Philadelphia, PA, Aug 2014. [vi](#), [2](#), [3](#), [16](#)

- [8] D.F. Geesaman, K Saito, and A Thomas. The nuclear emc effect. *Annual Review of Nuclear and Particle Science*, 45(1):337–390, 1995. 8
- [9] J. Gomez et al. Measurement of the A-dependence of deep inelastic electron scattering. *Phys. Rev.*, D49:4348–4372, 1994. 8, 26
- [10] D. Higinbotham. The emc effect still puzzles after 30 years - cern courier. <http://cerncourier.com/cws/article/cern/53091>, April 2013. (Visited on 01/04/2016). vi, 2, 7, 9
- [11] R Hofstadter. Nuclear and nucleon scattering of high-energy electrons. *Annual Review of Nuclear Science*, 7(1):231–316, 1957. 4
- [12] Henry W. Kendall. Deep inelastic scattering: Experiments on the proton and the observation of scaling. *Rev. Mod. Phys.*, 63:597–614, Jul 1991. 6
- [13] Simona Malace, David Gaskell, Douglas W. Higinbotham, and Ian Cloet. The Challenge of the EMC Effect: existing data and future directions. *Int. J. Mod. Phys.*, E23:1430013, 2014. 6
- [14] R. W. McAllister and R. Hofstadter. Elastic scattering of 188-mev electrons from the proton and the alpha particle. *Phys. Rev.*, 102:851–856, May 1956. 2
- [15] P R Norton. The emc effect. *Reports on Progress in Physics*, 66(8):1253, 2003. vi, 8
- [16] Bogdan Povh, Klaus Rith, Christoph Scholz, and Frank Zetsche. *Particles and Nuclei: An Introduction to the Physical Concepts*. Springer, 2009. 1, 2, 4, 5
- [17] Tom Powers, Lawrence Doolittle, Rok Ursic, and Jeffrey Wagner. Design, commissioning and operational results of wide dynamic range bpm switched electrode electronics. *AIP Conference Proceedings*, 390(1):257–265, 1997. 13, 22

- [18] J. Seely et al. New measurements of the european muon collaboration effect in very light nuclei. *Phys. Rev. Lett.*, 103:202301, Nov 2009. [2](#), [8](#), [9](#)
- [19] Richard E. Taylor. Deep inelastic scattering: The early years. *Rev. Mod. Phys.*, 63:573–595, Jul 1991. [6](#)
- [20] Hall A Tech. Ep method. http://hallaweb.jlab.org/equipment/beam/energy/ep_web.html. (Accessed on 06/28/2016). [16](#)
- [21] Pengjia Zhu et al. Beam Position Reconstruction for the g2p Experiment in Hall A at Jefferson Lab. *Nucl. Instrum. Meth.*, A808:1–10, 2016. [vi](#), [13](#), [14](#), [15](#), [22](#)

Appendix